ADVANCING EARTH AND SPACE SCIENCES

Geophysical Research Letters

RESEARCH LETTER

10.1029/2023GL106162

Key Points:

- Characterizing electron loss through peaks and minima in radial phase space density can misrepresent simultaneous loss mechanisms
- Analysis of electron loss across all adiabatic invariants μ, K, and L^*, is necessary to correctly identify loss mechanisms
- Observational analysis of phase space density data alone cannot be used to quantify individual contributions of simultaneous loss processes

Supporting Information:

Supporting Information may be found in the online version of this article.

Correspondence to:

F. A. Staples,
fastaples@atmos.ucla.edu

Citation:

Staples, F. A., Ma, Q., Kellerman, A., Rae, I. J., Forsyth, C., Sandhu, J. K., & Bortnik, J. (2023). Differentiating between simultaneous loss drivers in Earth's outer radiation belt: Multi-dimensional phase space density analysis. *Geophysical Research Letters*, *50*, e2023GL106162. https://doi.org/10.1029/2023GL106162

Received 31 AUG 2023
Accepted 18 SEP 2023

Author Contributions:

Conceptualization: F. A. Staples, I. J. Rae
Data curation: A. Kellerman
Formal analysis: F. A. Staples, Q. Ma, A. Kellerman, J. K. Sandhu
Investigation: F. A. Staples
Methodology: F. A. Staples, A. Kellerman
Resources: A. Kellerman
Software: F. A. Staples, Q. Ma
Supervision: A. Kellerman, I. J. Rae, C. Forsyth, J. Bortnik
Writing – original draft: F. A. Staples

Differentiating Between Simultaneous Loss Drivers in Earth's Outer Radiation Belt: Multi-Dimensional Phase Space Density Analysis

F. A. Staples[1], Q. Ma[1,2], A. Kellerman[1], I. J. Rae[3], C. Forsyth[4], J. K. Sandhu[3], and J. Bortnik[1]

[1]Department of Atmospheric and Oceanic Sciences, University of California, Los Angeles, Los Angeles, CA, USA, [2]Center for Space Physics, Boston University, Boston, MA, USA, [3]Department of Mathematics, Physics and Electrical Engineering, Northumbria University, Newcastle upon Tyne, UK, [4]Mullard Space Science Laboratory, University College London, London, UK

Abstract We analyzed the contribution of electromagnetic ion cyclotron (EMIC) wave driven electron loss to a flux dropout event in September 2017. The evolution of electron phase space density (PSD) through the dropout showed the formation of a radially peaked PSD profile as electrons were lost at high L^*, resembling distributions created by magnetopause shadowing. By comparing 2D Fokker Planck simulations of pitch angle diffusion to the observed change in PSD, we found that the μ and K of electron loss aligned with maximum scattering rates at dropout onset. We conclude that, during this dropout event, EMIC waves produced substantial electron loss. Because pitch angle diffusion occurred on closed drift paths near the last closed drift shell, no radial PSD minimum was observed. Therefore, the radial PSD gradients resembled solely magnetopause shadowing loss, even though the local pitch angle scattering produced electron losses of several orders of magnitude of the PSD.

Plain Language Summary Extremely energetic charged particles become trapped by Earth's geomagnetic field, forming the Van Allen radiation belts. The total amount of radiation trapped within these belts varies depending on the solar wind conditions, which can disturb the geomagnetic field to produce geomagnetic storms. At the beginning of a geomagnetic storm, there is a relative calm in the radiation belt, produced by the rapid drainage of electrons from the geomagnetic field. It is not fully understood if these electrons are primarily lost into the solar wind, or if they are lost into Earth's atmosphere. In this study, we analyze the remaining trapped electrons to reconstruct the mechanisms of electron escape at the beginning of a geomagnetic storm in September 2017. While previous work found that electrons were primarily lost into the solar wind, we found that loss into the atmosphere also played an important role. Furthermore, we showed that drainage of electrons into the atmosphere can be mistaken for loss into the solar wind if the energy and trajectory of lost electrons are not carefully considered.

1. Introduction

Relativistic electron flux in the outer radiation belt is highly variable, changing on timescales from seconds to years (e.g., Abel & Thorne, 1998; Mann & Ozeke, 2016; Nakamura et al., 2000). These changes are controlled by a variety of acceleration and loss mechanisms acting independently or in tandem (Friedel et al., 2002; Reeves et al., 2003; Ripoll et al., 2020). One of the fastest and most dramatic changes to electron flux is radiation belt flux dropouts, when trapped electron populations are observed to suddenly decrease by a factor of 50 or more at a wide range of L-shells, energies, and pitch angles (Pierrard et al., 2020; Turner, Morley, et al., 2012; Turner & Ukhorskiy, 2020; Xiang et al., 2018). Losses are either produced by wave-particle interactions which scatter electrons into the atmospheric loss cone (Horne & Thorne, 1998; Kennel & Petschek, 1966; Miyoshi et al., 2008; Thorne & Kennel, 1971), or through the magnetopause into interplanetary space, termed "magnetopause shadowing" (Green et al., 2004; X. Li et al., 1997; Morley et al., 2010; Shprits et al., 2006). The extent to which magnetopause shadowing and atmospheric precipitation each contribute to a radiation belt dropout has been a topic of continuing debate (e.g., Bortnik et al., 2006; Morley et al., 2010; Shprits et al., 2017; Staples et al., 2022; Turner, Shprits, et al., 2012; Turner et al., 2014; Xiang et al., 2017; Zhang et al., 2016).

Writing – review & editing: F. A. Staples, Q. Ma, A. Kellerman, I. J. Rae, C. Forsyth, J. K. Sandhu

A useful tool to distinguish loss mechanisms is phase space density (PSD) analysis of electron dynamics in adiabatic invariant coordinates (μ, K, L^*), which reveal non-adiabatic changes to electron populations (e.g., Degeling et al., 2008; Green & Kivelson, 2004; Selesnick & Blake, 2000). Magnetopause shadowing is typically characterized by PSD loss outside of the last closed drift shell (LCDS), where electron drift paths intersect the magnetopause, followed by diffusive transport across radial gradients in L^* toward the magnetopause (Loto'aniu et al., 2010; Shprits et al., 2006; Turner, Shprits, et al., 2012). This process creates a localized peak in radial PSD profiles during flux dropouts (illustrated by Turner, Shprits, et al., 2012). Precipitation to the atmosphere is characterized by PSD loss at a localized L^*, which may create a minimum in radial PSD profiles (Aseev et al., 2017; Blum et al., 2020; Capannolo et al., 2018; Shprits et al., 2017, 2018). A local minimum in PSD must be observed to deepen over time to interpret with certainty that precipitation produces PSD loss, rather than magnetopause shadowing followed by inward radial diffusion. Hence, satellite observations over multiple orbits are usually required to attribute loss observations to localized precipitation. Xiang et al. (2017) discussed how observations of PSD at a wide range of μ and K, for a given L^*, provide credible clues to the dominant mechanism of electron loss. For example, EMIC wave scattering of electrons into the loss cone results in depletions at μ and K values associated with electron energies resonant with EMIC waves (Drozdov et al., 2022; X. Ma et al., 2020; Xiang et al., 2018).

In this work, we investigated the dependence of PSD loss over a wide range of μ and K during an electron flux dropout which took place in September 2017, following an extreme magnetospheric compression. Staples et al. (2022) previously identified that magnetopause shadowing was the dominant mechanism of electron loss during this dropout, based upon the evolution of PSD characteristics as a function of L^*. However, such extreme magnetospheric compressions are also known drivers of EMIC wave generation (Anderson & Hamilton, 1993; Engebretson et al., 2002; Usanova et al., 2008; Xue et al., 2021). This paper aims to understand if localized precipitation into the atmosphere was appreciable during the dropout by analyzing PSD loss at a wide range of μ and K values.

2. Data and Methodology

2.1. Phase Space Density Data Set

PSD observations between 7 and 9 September 2017 were taken from 32 individual satellites which are part of five different scientific missions and hosted payloads. This data set achieves the highest temporal and spatial resolution of existing combined PSD observations of the radiation belt:

- Van Allen Probe Magnetic Electron Ion Spectrometer (MagEIS) and Relativistic Electron-Proton Telescope (REPT) instruments (Baker et al., 2014; Blake et al., 2014). 2 probes.
- GOES 13, 15 (Geostationary Operational Environmental Satellite) Magnetospheric Electron Detector (MAGED) Energetic Proton, Electron, and Alpha Detector (EPEAD) (Rodriguez, 2014a, 2014b; Sillanpää et al., 2017). 2 probes.
- GPS (Global Positioning System) Navstar Combined X-ray Dosimeter (CXD) (Tuszewski et al., 2004). 21 probes.
- THEMIS (Time History of Events and Macroscale Interactions during Substorms) Electrostatic Analyzer (ESA) and Solid State Telescope (SST) (Angelopoulos, 2008; Angelopoulos et al., 2008; McFadden et al., 2008). 3 Probes.
- MMS (Magnetospheric Multiscale) Fly's Eye Electron Proton Spectrometer (FEEPS) (Blake et al., 2016; Burch et al., 2016). 4 probes.

Intercalibrations between satellites were completed following Staples et al. (2022). All spacecraft data is calibrated to Van Allen Probe B and bias corrected GOES 15 data, which are chosen as "gold standard." In this work GPS pitch angle distributions were assumed using the Zhao et al. (2018) model. For each spacecraft instrument, the adiabatic invariants μ, K, and L^* were computed using a either a realistic magnetospheric field model, represented by the International Geomagnetic Reference Field model (IGRF; Thébault et al., 2015) and Tsyganenko (1989) external magnetic field model (T89), or a dipolar field configuration.

2.2. 2D Fokker Planck Diffusion Simulation

We used the Full Diffusion Code at University of California, Los Angeles, to calculate the electron diffusion coefficients due to EMIC waves (Q. Ma et al., 2019). The magnetic power spectra of EMIC waves were measured by the Electric and Magnetic Field Instrument Suite and Integrated Science (EMFISIS; Kletzing et al., 2013) instrument on Van Allen Probe B. Diffusion coefficients were calculated for six separate EMIC wave observations, each selected based upon EMIC wave power spectrogram over 30-min windows through the dropout interval, 00–03 UT on 8 September 2017 (see Figure 2), summarized in Table S1 in Supporting Information S1. The EMIC wave normal angle distribution was assumed to change from quasi-field aligned at the equator to more oblique at higher latitudes, according to the latitudinally-varying model in Ni et al. (2015). The latitude of the wave power was assumed to span from the equator to 40°, and below the latitude where the wave frequency equals the crossover frequency. We considered three ion species with composition ratios of 70% H^+, 20% He^+, and 10% O^+ (Meredith et al., 2003), and multiple harmonic resonances (up to 5 orders) and Landau resonance between electrons and EMIC waves. Electron scattering by hiss waves was incorporated into diffusion coefficients by using the statistical hiss wave frequency spectrum (W. Li et al., 2015). The diffusion coefficients due to hiss waves were much smaller than those due to EMIC waves at energies above 1 MeV, except for the high pitch angles close to 90°.

After the bounce-averaged diffusion coefficients were computed, we performed 2D Fokker Planck simulations of the electron PSD evolution due to the resonant interaction with EMIC waves. The 2D Fokker Planck equation was numerically solved using the Alternative Direction Implicit method (Q. Ma et al., 2012). The initial conditions and boundary conditions used in the simulation are detailed in Text S1 in Supporting Information S1. The simulation was performed for 4-hr using the observed EMIC wave amplitudes. The electron PSD at each energy decreased exponentially with time shortly after the simulation starts. The time scale of the exponential decay corresponds to the electron lifetime, which is energy dependent. The simulated electron PSD evolution was not directly compared with observed dropouts because the MLT coverage of EMIC waves is uncertain. As will be shown in the following analysis, we compared the simulated μ and K dependences of electron PSD decay with the observation, after transforming the pitch angle and energy dependence into the adiabatic invariant coordinates for a dipolar magnetic field.

3. Event Analysis

The compound geomagnetic storm between 7–9 September 2017 was driven by a sequence of interacting coronal mass ejecta (CME) and interplanetary shocks traveling through the solar wind (Scolini et al., 2020; Shen et al., 2018; Werner et al., 2019). Figure 1 summarizes the radiation belt response to the solar wind and the subsequent geomagnetic conditions. At 23 UT on 7 September, an interplanetary shock arrived at the magnetosphere, indicated by the sudden increase in IMF field strength to 33 nT with a decrease of the B_z component to −31 nT (Figure 1a), and solar wind speed increases to 830 km s^{-1} (Figure 1b). As a result, the magnetopause was compressed within geostationary orbit (purple crosses, Figure 1c) and the Sym-H index suddenly decreased to −142 nT, indicating storm onset followed by the main phase. Through the main phase of the storm (23 UT 7 September–01 UT 8 September), electron PSD decreased suddenly by up to three orders of magnitude (for μ = 1,000 MeV/G and K = 0.1 $G^{0.5}R_E$, Figure 1e). Through the recovery phase of the storm the PSD remained low compared to pre-storm PSD, until 12 UT on 8 September when PSD increased substantially through localized electron acceleration (Staples et al., 2022).

Figures 1i–1iv show radial PSD profiles during the dropout between 23 UT on 7 September–03 UT on 8 September for μ = 1,000 MeV/G and K = 0.1 $G^{0.5}R_E$. Each panel compares the hourly averaged PSD to the average pre-storm PSD between 17 and 21 UT on 7 September (gray profiles). Immediately prior to the dropout, between 23 and 24 UT on 7 September, the PSD at $L^* < 4$ was, on average, slightly greater than the pre-storm PSD. At the onset of the dropout during the following hour (Figure 1ii), PSD measurements at $L^* > 3.7$ were up to three orders of magnitude less than pre-storm PSD, with greater losses at higher L^*. Between 01 and 02 UT on 8 September (Figure 1iii) loss continued to occur at $L^* > 3.7$; the maximum PSD loss was measured to be over three orders of magnitude compared to pre-storm PSD at $L^* = 4.4$. The final interval 02–03 UT on 8 September (Figure 1iv) showed the PSD was approximately the same as the pre-storm PSD at $L^* < 3.6$, whereas PSD had decreased by over two orders of magnitude compared the pre-storm PSD at $L^* > 3.6$, with greatest loss occurring at high $L^* = 4.4$. PSD at $L^* > 4$ increased substantially between 02 and 03 UT on 8 September (interval iv) compared to the previous hour (interval iii).

Figures 1i–1iv shows the formation of a radial PSD peak at $L^* \sim 3.7$ following an incursion of the LCDS, with greatest electron losses observed at $L^* > 3.7$. These characteristics appear consistent with electron loss to the compressed magnetopause, and outward radial diffusion, as concluded by Staples et al. (2022).

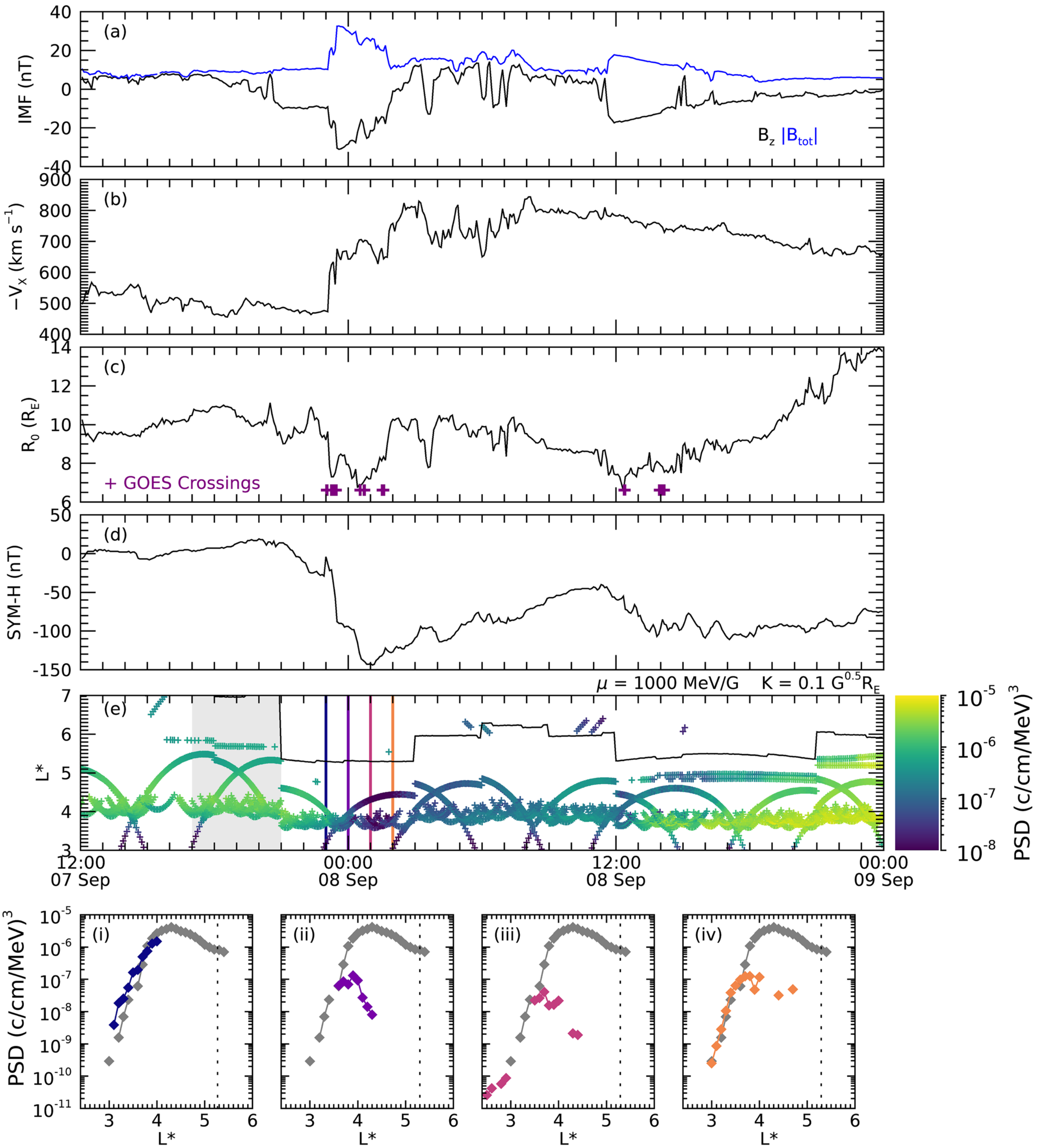

Figure 1. Panels (a)–(e) summarize the solar wind, geomagnetic, and radiation belt conditions between 12 UT 7 September and 00 UT 9 September 2017: (a) interplanetary magnetic field strength (blue) and B_z component (black); (b) solar wind speed; (c) subsolar magnetopause (black line, Shue et al., 1998) and radial distance to GOES magnetopause crossings (purple crosses); (d) Sym-H index; (e) PSD of electrons at $\mu = 1{,}000$ MeV/G and $K = 0.1\ \mathrm{G}^{0.5}R_\mathrm{E}$. Panels (i–iv) show radial PSD profiles. The gray profile on all panels references the average pre-storm PSD, the colored profiles show hourly PSD through the dropout, the beginning time of each hour is indicated by correspondingly colored vertical lines in panel (e). The location of the LCDS is indicated by the black line in panel (e) and vertical dashed lines in panels (i–iv).

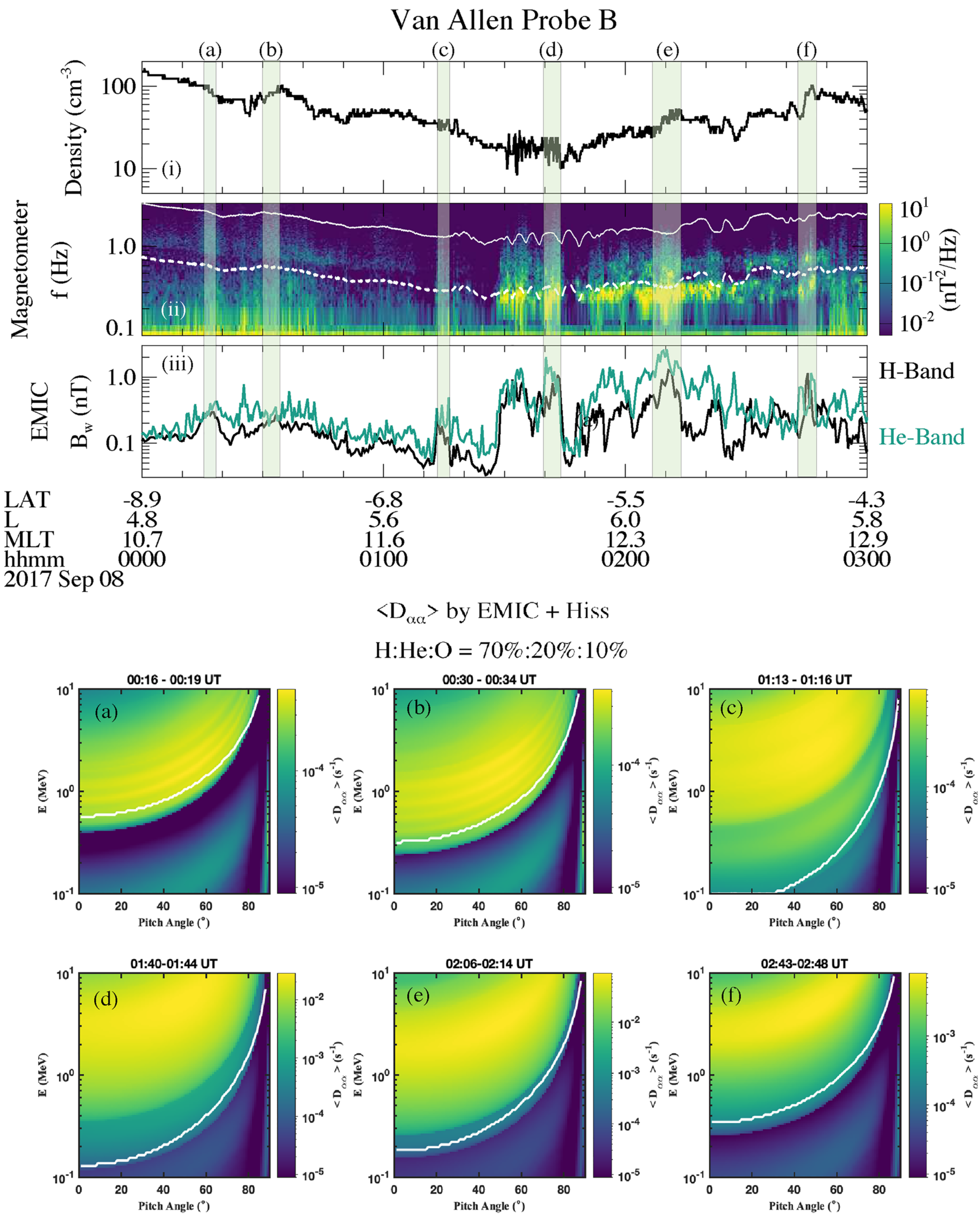

Figure 2. Van Allen Probe B observation of EMIC waves and the bounce-averaged diffusion coefficients. (i) Total electron density; (ii) magnetic wave power spectrogram, where the white solid and dashed lines are equatorial ion gyrofrequencies f_{cp} and f_{cHe}, respectively; (iii) H^+ band and He^+ band EMIC wave amplitudes. Green shaded boxes over (i)–(iii) indicate the times of EMIC wave samples (a–f). Pitch angle diffusion coefficients, $D_{\alpha\alpha}$, computed from statistical hiss and sampled EMIC waves are displayed as a function of energy and pitch angle in panels (a–f). White lines in panels (a–f) indicate minimum resonant energies between electrons and EMIC waves.

To analyze whether localized precipitation to the atmosphere contributed to electron loss during the dropout, we searched for EMIC wave signatures using EMFISIS observations of the magnetic power spectra. Strong EMIC waves were identified during the flux dropout, between 00 and 03 UT on 8 September, observed by Van Allen Probe B on an outbound orbit toward apogee at noon, summarized in Figure 2. Figure 2i shows that the total electron density was between 10 and 100 cm^{-3}, and significant power spectral density was observed below the equatorial H^+ and He^+ gyrofrequencies (Figure 2ii), indicating the presence of H^+ band and He^+ band EMIC waves. The integrated wave amplitude of the H^+ and He^+ frequency wave bands (Figure 2iii) show that He^+ band waves were higher in amplitude throughout the interval, with the largest amplitude waves observed between 01:300 and 02:30 UT 8 September, reaching a maximum amplitude of >2 nT in the He^+ band and >1 nT in the H^+ band.

Figures 2a–2f show bounce averaged electron pitch angle diffusion coefficients, $D_{\alpha\alpha}$, computed using the averaged EMIC wave spectra of the observed wave bursts (labeled on panels i–iii) and statistical hiss wave spectra. Figures 2a–2f show that EMIC waves could interact with electrons at very low energies in the ∼100 s of keV range for equatorial electrons with pitch angles <70° and ∼MeV range for electrons with equatorial pitch angles >70°. The high EMIC wave power in the He^+ band between 01:30 and 02:30 UT resulted in extremely high pitch angle diffusion coefficients of >0.001 s^{-1} for electron energies >400 keV and pitch angles <70°. While diffusion timescales of electrons varied greatly upon energy and pitch angles, Figure 2 nonetheless demonstrates that EMIC wave-particle interactions could produce rapid diffusion of electrons toward the loss cone during the dropout.

Figure 3 compares the simulated change in electron PSD during the dropout (Figures 3a–3f, left column) to the observed change in PSD (Figures 3g–3l, right column) as a function of μ and K. Each row shows the simulated and observed df for the case of each 30-min window during the dropout period, where df is described by Equation 1. Because simulations of df were conducted in a dipolar magnetic field, PSD observations presented in Figure 3 were also converted into adiabatic coordinates using a dipolar magnetic field to allow for comparison.

$$df = \log_{10}\left(\frac{\text{Dropout PSD}}{\text{Pre} - \text{storm PSD}}\right) \tag{1}$$

For the case of both simulated and observed df, "Pre-storm PSD" was set to average Van Allen Probe B observation between 17 and 21 UT on 7 September (gray shaded area Figure 1e). For simulated df, the "Dropout PSD" for each 30-min window was determined by a 2D Fokker-Plank simulation of electron diffusion which used diffusion coefficients calculated from sampled EMIC wave spectra (see Figure 2) and statistical hiss wave spectra (described in Section 2.2). The initial condition of this simulation was equal to the "Pre-storm PSD." The final simulated PSD values were determined when the 2 MeV electron PSD matched the average PSD sampled by Van Allen Probe B during the 30-min window. For the case of observed df, "Dropout PSD" was the PSD averaged over 30-min windows between 00 and 03 UT on 8 September (between purple-orange lines Figure 1e). Note that the observed L range overlapped between windows because a wide sample of electron pitch angles is considered as the probe follows an outbound orbit.

Figure 3 shows that PSD decreased ($df < 0$) compared to the pre-storm interval at nearly all μ and K values across the phase space, and PSD decrease exemplified pitch angle scattering loss instead of magnetopause shadowing effects: Throughout the dropout the magnitude of PSD loss was observed to be highly dependent on μ and K, with maximum PSD loss (white dots) showed a non-linear relationship between μ and K, corresponding to the energy and pitch angle dependent loss mechanism. At the onset of the dropout, between 00 and 01 UT (Figures 3a and 3b), the μ and K values of maximum observed PSD loss aligned with the maximum simulated PSD loss for EMIC wave scattering. This serves as compelling evidence that PSD loss was produced by EMIC wave scattering between $4.46 < L < 5.42$.

Observations between 01 and 02 UT showed the greatest PSD decrease through the orbit of Van Allen Probe B (Figures 3i and 3j), with $df < 3$ for $\mu \sim 600$ MeV/G and $K \sim 0.2\ G^{0.5}R_E$. While the maximum PSD loss after 01 UT followed a similar relationship between μ and K as earlier in the dropout, the maximum observed df did not coincide with simulated df through EMIC wave scattering. The simulated df estimated that maximum PSD loss would occur at very high μ (multi-MeV), corresponding to energy channels where electron flux was measured at the instrument noise floor (above dashed white line). Nonetheless, simulated PSD loss showed that EMIC waves were capable of scattering electrons at μ and K below the noise floor by similar orders of magnitude as Van Allen Probe B observations. There could be several reasons why the maximum observed PSD loss after 01 UT did not

10.1029/2023GL106162

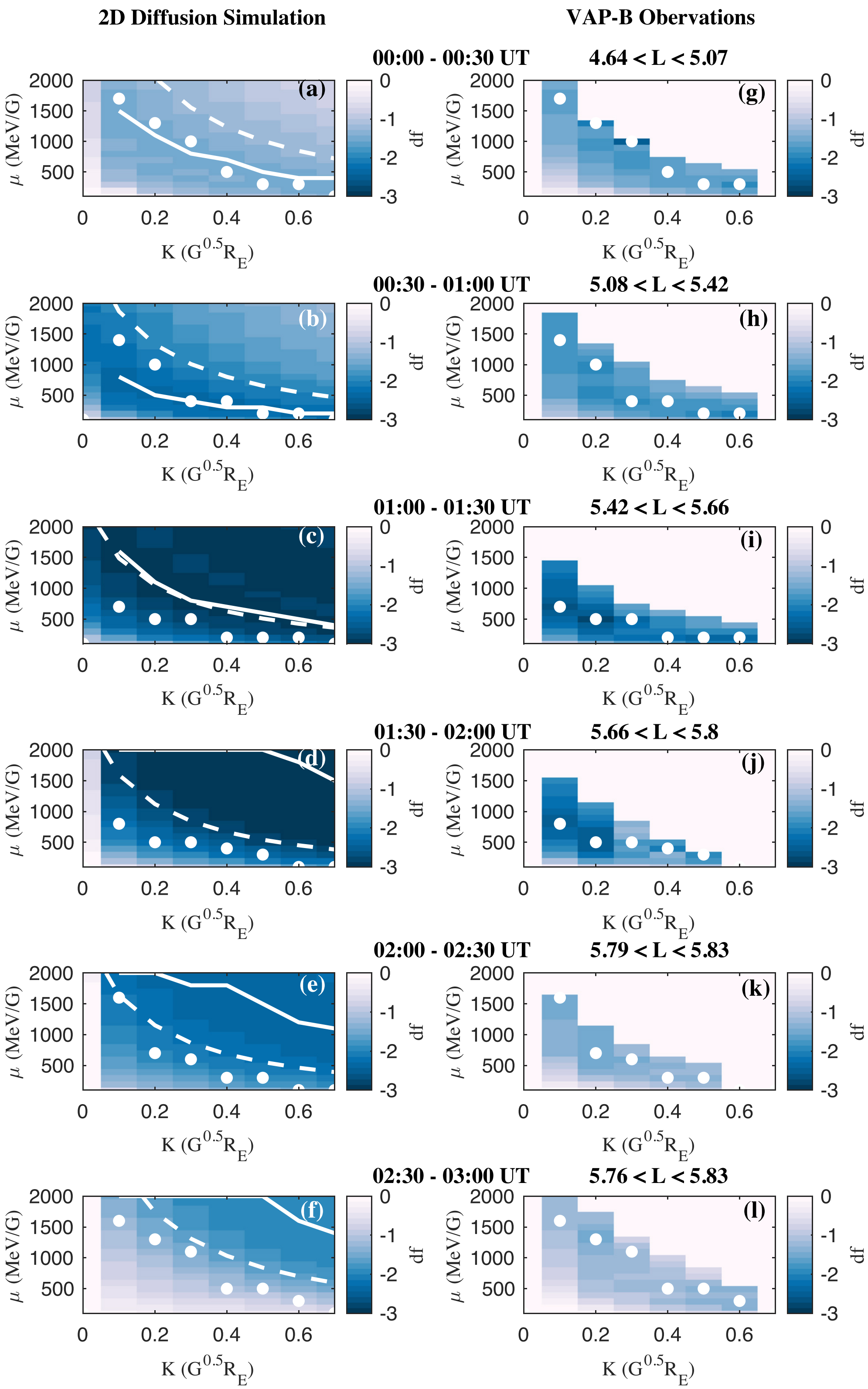

Figure 3.

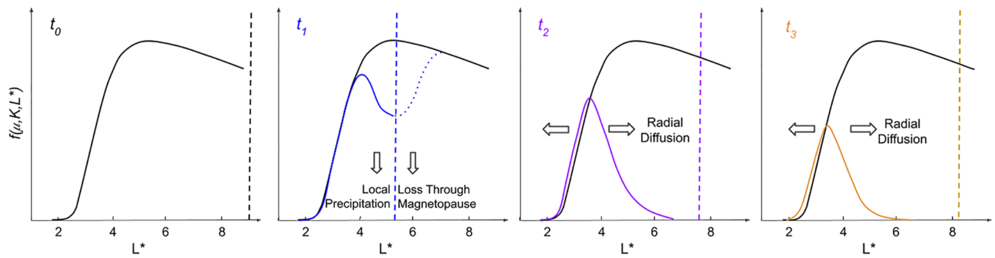

Figure 4. Diagram of PSD evolution over four time periods $t_0 - t_3$ (left to right) as a function of L^* for a scenario where magnetopause shadowing produces electron loss on open drift paths, and EMIC wave-particle interactions produce fast precipitation to the atmosphere inside of the LCDS. Vertical dashed lines represent the LCDS. The blue dotted line in panel t_1 illustrates PSD profile if local precipitation acted alone to produce a localized PSD loss.

align in μ and K with the maximum simulated PSD loss, such as inaccuracies in the assumptions made when calculating simulation diffusion coefficients. For example, the EMIC waves with a different frequency spectrum from that observed by Van Allen Probe B in Figure 2ii could occur at other MLT sectors or times which were not sampled by the satellite. Furthermore, an assumed ion composition ratio was used, which could alter the energy and pitch angle dependence of pitch angle diffusion (Kang et al., 2015).

Observations between 02 and 03 UT (Figures 3k and 3l) show that $|df|$ was smaller than the previous hour (Figures 3i and 3j) at all μ and K. This shows that acceleration processes acted to produce a net-increase in PSD after ~02 UT compared to the previous hour, which is supported by high resolution multi-mission PSD observations presented in Figure 1iii–1iv. Because acceleration also produced changes to observed df during this hour, we cannot differentiate the effects of EMIC wave scattering across all μ and K.

4. Conclusion

This study examined the characteristics of electron loss induced by EMIC wave-particle interactions by considering changes to electron PSD as a function of the first and second adiabatic invariants. In the event analyzed in September 2017, an electron flux dropout was produced following a strong magnetospheric compression and geomagnetic storm. Previous work identified magnetopause shadowing as the dominant loss mechanism through analysis of radial PSD profiles across L^* (Staples et al., 2022). In our analysis, we also found that the evolution of radial PSD profiles through the dropout interval showed characteristics of magnetopause shadowing; a radial PSD peak was formed following an incursion of the LCDS, and no PSD minima were observed to deepen over time (Figures 1i–1iv). However, observations from Van Allen Probe B showed significant wave power in both H^+ and He^+ EMIC wave bands between 0 and 3 UT on 8 September. Simultaneously, Van Allen Probe B observed concurrent electron PSD loss by up to three orders of magnitude compared to the pre-storm interval (Figure 3). We found that observed PSD loss was closely reproduced by a 2D Fokker-Plank simulation which modeled diffusion by sampled EMIC wave observations, and statistical hiss waves, at the onset of the dropout 00–01 UT 8 September (Figures 3a–3b, 3g–3h). PSD loss observed during the latter part of the dropout was found to be more difficult to analyze through simulation because the electron fluxes were reduced to the instrument noise floor, limiting PSD observations at high energies. Nonetheless, the observations of PSD loss at dropout onset provided compelling evidence that EMIC wave driven electron scattering contributed to electron loss for electrons at $L^* > 4$.

We argue that during this flux dropout event, EMIC wave-particle interactions produced electron loss on closed drift paths, whereas magnetopause shadowing produced electron loss on open drift paths beyond the LCDS. Figure 4 provides an illustration of PSD evolution for this scenario: At time t_0 the PSD profile represents a pre-storm distribution which is radially peaked at $L^* = 5$. Time t_1 represents a period of strong magnetospheric compression which causes the LCDS to decrease to low L^*, and EMIC waves are generated in the outer

Figure 3. Left Column (a–f) shows simulated change in PSD, *df*, based upon EMIC wave observations sampled over 30-min windows during the PSD dropout between 00 UT 8 September and 03 UT 8 September. Right column (g–l) shows corresponding Van Allen Probe B observations of average PSD change, *df*, over each window. Observed and simulated *df* are shown by color as a function of μ and K, approximated in a dipolar magnetic field. Solid white lines/dots show the values of maximum simulated/observed PSD loss (minimum *df*) as a function of μ. The dashed white line indicates the maximum measurable μ after taking the noise floor into consideration.

magnetosphere, near the LCDS. As a result, electrons on open drift paths beyond the LCDS are lost across the magnetopause, and on closed drift paths EMIC waves drive rapid pitch angle diffusion and subsequent loss to the atmosphere. The location of the LCDS relative to EMIC wave activity obscures any radial PSD minimum created by local precipitation. Time t_2 represents a relaxation of the magnetosphere, and the LCDS increases to higher L^*. Combined losses to the magnetopause and atmosphere at high L^* result in a localized peak in PSD and steep radial PSD gradients. Time t_3 represents how ULF wave driven radial diffusion could act to smooth radial gradients produced by losses. This scenario demonstrates that simultaneous loss processes at high L^* result in a PSD evolution which was previously interpreted as magnetopause loss only. Only when analyzing PSD loss as a function of μ and K do EMIC wave-particle interaction characteristics come to light.

It is an unexpected finding that local wave-particle interactions could be an effective loss mechanism near the LCDS for two reasons: First, EMIC wave interactions typically produce scattering of ∼MeV electrons (Usanova et al., 2014), but the observed loss was across a wide range of radiation belt energies >100 s keV. Second, efficient electron scattering by EMIC waves usually occurs in the overlapped region of the ring current and the high-density plasmasphere, where the minimum resonance energy is reduced (Meredith et al., 2003; Summers et al., 2007). In the September 2017, the drainage of electrons into the outer magnetosphere during the main phase of the geomagnetic storm (Figure 2i) provided higher than usual plasma density in the outer magnetosphere, allowing EMIC waves to interact with lower energy electrons (100 s of keV). In addition, the magnetosphere was extremely compressed (Figure 1c), so the LCDS was located at low L^* relative to localized EMIC wave-particle interactions. This is an important finding because the conclusion is contrary to the previous understanding that a negative gradient in PSD toward the LCDS is indicative of magnetopause shadowing loss.

Data Availability Statement

Multi-mission phase space density observations presented in this study are publicly available via https://doi.org/10.5281/zenodo.7293955. Spacecraft data from GOES and the Van Allen Probes are publicly available via the NASA/GSFC CDAWeb service (https://cdaweb.gsfc.nasa.gov/index.html/). Solar Wind data and geomagnetic indices are publicly available through the NASA/GSFC Space Physics Data Facility OMNIWeb service (https://omniweb.gsfc.nasa.gov/).

Acknowledgments

We acknowledge the developers of the IRBEM library, which was used to compute adiabatic invariant coordinates (Boscher et al., 2013). The computations employed computational and storage services associated with the Hoffman2 Shared Cluster provided by UCLA Institute for Digital Research and Education's Research Technology Group. ACK acknowledges high-performance computing support from Cheyenne (https://doi.org/10.5065/D6RX99HX) provided by NCAR's Computational and Information Systems Laboratory, sponsored by the National Science Foundation. FS was supported by NASA Grant 80NSSC20K1402 and NSF Grant 2149782. ACK acknowledges support from NASA Grants 80NSSC20K1402 and 80NSSC20K1281, and NSF Grant 2149782. QM acknowledges the NASA Grant 80NSSC20K0196, and NSF Grant AGS-2225445. IJR and JKS acknowledge support from NERC Grants NE/P017185/2, NE/V002554/2, and STFC Grant ST/V006320/1. CF was supported by NERC IRF NE/N014480/1 and NERC Grants NE/P017185/1 and NE/V002554/2.

References

Abel, B., & Thorne, R. M. (1998). Electron scattering loss in Earth's inner magnetosphere: 1. Dominant physical processes. *Journal of Geophysical Research*, *103*(A2), 2385–2396. https://agupubs.onlinelibrary.wiley.com/doi/abs/10.1029/97JA02919

Anderson, B. J., & Hamilton, D. C. (1993). Electromagnetic ion cyclotron waves stimulated by modest magnetospheric compressions. *Journal of Geophysical Research*, *98*(A7), 11369–11382. https://agupubs.onlinelibrary.wiley.com/doi/abs/10.1029/93JA00605

Angelopoulos, V. (2008). The THEMIS mission. *Space Science Reviews*, *141*(1), 5–34. https://doi.org/10.1007/s11214-008-9336-1

Angelopoulos, V., Sibeck, D., Carlson, C. W., McFadden, J. P., Larson, D., Lin, R. P., et al. (2008). First results from the THEMIS mission. *Space Science Reviews*, *141*(1), 453–476. https://doi.org/10.1007/s11214-008-9378-4

Aseev, N. A., Shprits, Y. Y., Drozdov, A. Y., Kellerman, A. C., Usanova, M. E., Wang, D., & Zhelavskaya, I. S. (2017). Signatures of ultrarelativistic electron loss in the heart of the outer radiation belt measured by Van Allen Probes. *Journal of Geophysical Research: Space Physics*, *122*(10), 10102–10111. https://doi.org/10.1002/2017JA024485

Baker, D. N., Kanekal, S. G., Hoxie, V. C., Batiste, S., Bolton, M., Li, X., et al. (2014). The relativistic electron-proton telescope (REPT) instrument on board the radiation belt storm probes (RBSP) spacecraft: Characterization of Earth's radiation belt high-energy particle populations. In N. Fox & J. L. Burch (Eds.), *The Van Allen Probes mission* (pp. 337–381). Springer US.

Blake, J. B., Carranza, P. A., Claudepierre, S. G., Clemmons, J. H., Crain, W. R., Dotan, Y., et al. (2014). The magnetic electron ion spectrometer (MagEIS) instruments aboard the radiation belt storm probes (RBSP) spacecraft. In N. Fox & J. L. Burch (Eds.), *The Van Allen Probes mission* (pp. 383–421). Springer US.

Blake, J. B., Mauk, B. H., Baker, D. N., Carranza, P., Clemmons, J. H., Craft, J., et al. (2016). The fly's eye energetic particle spectrometer (FEEPS) sensors for the magnetospheric multiscale (MMS) mission. *Space Science Reviews*, *199*(1–4), 309–329. https://doi.org/10.1007/s11214-015-0163-x

Blum, L. W., Remya, B., Denton, M. H., & Schiller, Q. (2020). Persistent EMIC wave activity across the nightside inner magnetosphere. *Geophysical Research Letters*, *47*(6), e2020GL087009. https://doi.org/10.1029/2020GL087009

Bortnik, J., Thorne, R. M., O'Brien, T. P., Green, J. C., Strangeway, R. J., Shprits, Y. Y., & Baker, D. N. (2006). Observation of two distinct, rapid loss mechanisms during the 20 November 2003 radiation belt dropout event. *Journal of Geophysical Research*, *111*(A12), A12216. https://agupubs.onlinelibrary.wiley.com/doi/abs/10.1029/2006JA011802

Boscher, D., Bourdarie, S., O'Brien, T. P., & Guild, T. (2013). The international radiation belt environment modeling (IRBEM) library.

Burch, J. L., Moore, T. E., Torbert, R. B., & Giles, B. L. (2016). Magnetospheric multiscale overview and science objectives. *Space Science Reviews*, *199*(1), 5–21. https://doi.org/10.1007/s11214-015-0164-9

Capannolo, L., Li, W., Ma, Q., Zhang, X.-J., Redmon, R. J., Rodriguez, J. V., et al. (2018). Understanding the driver of energetic electron precipitation using coordinated multisatellite measurements. *Geophysical Research Letters*, *45*(14), 6755–6765. https://doi.org/10.1029/2018GL078604

Degeling, A. W., Ozeke, L. G., Rankin, R., Mann, I. R., & Kabin, K. (2008). Drift resonant generation of peaked relativistic electron distributions by Pc 5 ULF waves. *Journal of Geophysical Research*, *113*(A2), A02208. https://doi.org/10.1029/2007JA012411

Drozdov, A. Y., Allison, H. J., Shprits, Y. Y., Usanova, M. E., Saikin, A., & Wang, D. (2022). Depletions of multi-MeV electrons and their association to minima in phase space density. *Geophysical Research Letters*, *49*(8), e2021GL097620. https://doi.org/10.1029/2021GL097620

Engebretson, M. J., Peterson, W. K., Posch, J. L., Klatt, M. R., Anderson, B. J., Russell, C. T., et al. (2002). Observations of two types of Pc 1–2 pulsations in the outer dayside magnetosphere. *Journal of Geophysical Research*, *107*(A12), SMP20-1–SMP20-20. https://agupubs.onlinelibrary.wiley.com/doi/abs/10.1029/2001JA000198

Friedel, R. H. W., Reeves, G. D., & Obara, T. (2002). Relativistic electron dynamics in the inner magnetosphere — A review. *Journal of Atmospheric and Solar-Terrestrial Physics*, *64*(2), 265–282. https://doi.org/10.1016/s1364-6826(01)00088-8

Green, J. C., & Kivelson, M. G. (2004). Relativistic electrons in the outer radiation belt: Differentiating between acceleration mechanisms. *Journal of Geophysical Research*, *109*(A3), A03213. https://agupubs.onlinelibrary.wiley.com/doi/abs/10.1029/2003JA010153

Green, J. C., Onsager, T. G., O'Brien, T. P., & Baker, D. N. (2004). Testing loss mechanisms capable of rapidly depleting relativistic electron flux in the Earth's outer radiation belt. *Journal of Geophysical Research*, *109*(A12), A12211. https://agupubs.onlinelibrary.wiley.com/doi/abs/10.1029/2004JA010579

Horne, R. B., & Thorne, R. M. (1998). Potential waves for relativistic electron scattering and stochastic acceleration during magnetic storms. *Geophysical Research Letters*, *25*(15), 3011–3014. https://agupubs.onlinelibrary.wiley.com/doi/abs/10.1029/98GL01002

Kang, S.-B., Min, K.-W., Fok, M.-C., Hwang, J., & Choi, C.-R. (2015). Estimation of pitch angle diffusion rates and precipitation time scales of electrons due to EMIC waves in a realistic field model. *Journal of Geophysical Research: Space Physics*, *120*(10), 8529–8546. https://doi.org/10.1002/2014JA020644

Kennel, C. F., & Petschek, H. E. (1966). Limit on stably trapped particle fluxes. *Journal of Geophysical Research*, *71*(1), 1–28. https://agupubs.onlinelibrary.wiley.com/doi/abs/10.1029/JZ071i001p00001

Kletzing, C. A., Kurth, W. S., Acuna, M., MacDowall, R. J., Torbert, R. B., Averkamp, T., et al. (2013). The electric and magnetic field instrument suite and integrated science (EMFISIS) on RBSP. *Space Science Reviews*, *179*(1), 127–181. https://doi.org/10.1007/s11214-013-9993-6

Li, W., Ma, Q., Thorne, R. M., Bortnik, J., Kletzing, C. A., Kurth, W. S., et al. (2015). Statistical properties of plasmaspheric hiss derived from Van Allen Probes data and their effects on radiation belt electron dynamics. *Journal of Geophysical Research: Space Physics*, *120*(5), 3393–3405. https://doi.org/10.1002/2015JA021048

Li, X., Baker, D. N., Temerin, M., Cayton, T. E., Reeves, E. G. D., Christensen, R. A., et al. (1997). Multisatellite observations of the outer zone electron variation during the November 3–4, 1993, magnetic storm. *Journal of Geophysical Research*, *102*(A7), 14123–14140. https://agupubs.onlinelibrary.wiley.com/doi/abs/10.1029/97JA01101

Loto'aniu, T. M., Singer, H. J., Waters, C. L., Angelopoulos, V., Mann, I. R., Elkington, S. R., & Bonnell, J. W. (2010). Relativistic electron loss due to ultralow frequency waves and enhanced outward radial diffusion. *Journal of Geophysical Research*, *115*(A12), A12245. https://doi.org/10.1029/2010JA015755

Ma, Q., Li, W., Yue, C., Thorne, R. M., Bortnik, J., Kletzing, C. A., et al. (2019). Ion heating by electromagnetic ion cyclotron waves and magnetosonic waves in the Earth's inner magnetosphere. *Geophysical Research Letters*, *46*(12), 6258–6267. https://doi.org/10.1029/2019GL083513

Ma, Q., Ni, B., Tao, X., & Thorne, R. M. (2012). Evolution of the plasma sheet electron pitch angle distribution by whistler-mode chorus waves in non-dipole magnetic fields. *Annals of Geophysics*, *30*(4), 751–760. https://doi.org/10.5194/angeo-30-751-2012

Ma, X., Xiang, Z., Ni, B., Fu, S., Cao, X., Hua, M., et al. (2020). On the loss mechanisms of radiation belt electron dropouts during the 12 September 2014 geomagnetic storm. *Earth and Planetary Physics*, *4*(6), 598–610. https://agupubs.onlinelibrary.wiley.com/doi/abs/10.26464/epp2020060

Mann, I. R., & Ozeke, L. G. (2016). How quickly, how deeply, and how strongly can dynamical outer boundary conditions impact Van Allen radiation belt morphology? *Journal of Geophysical Research: Space Physics*, *121*(6), 5553–5558. https://doi.org/10.1002/2016JA022647

McFadden, J. P., Carlson, C. W., Larson, D., Ludlam, M., Abiad, R., Elliott, B., et al. (2008). The THEMIS ESA plasma instrument and in-flight calibration. *Space Science Reviews*, *141*(1), 277–302. https://doi.org/10.1007/s11214-008-9440-2

Meredith, N. P., Thorne, R. M., Horne, R. B., Summers, D., Fraser, B. J., & Anderson, R. R. (2003). Statistical analysis of relativistic electron energies for cyclotron resonance with EMIC waves observed on CRRES. *Journal of Geophysical Research*, *108*(A6), 1250. https://agupubs.onlinelibrary.wiley.com/doi/abs/10.1029/2002JA009700

Miyoshi, Y., Sakaguchi, K., Shiokawa, K., Evans, D., Albert, J., Connors, M., & Jordanova, V. (2008). Precipitation of radiation belt electrons by EMIC waves, observed from ground and space. *Geophysical Research Letters*, *35*(23), L23101. https://doi.org/10.1029/2008GL035727

Morley, S. K., Friedel, R. H. W., Spanswick, E. L., Reeves, G. D., Steinberg, J. T., Koller, J., et al. (2010). Dropouts of the outer electron radiation belt in response to solar wind stream interfaces: Global positioning system observations. *Proceedings of the Royal Society A: Mathematical, Physical and Engineering Sciences*, *466*(2123), 3329–3350. https://doi.org/10.1098/rspa.2010.0078

Nakamura, R., Isowa, M., Kamide, Y., Baker, D. N., Blake, J. B., & Looper, M. (2000). SAMPEX observations of precipitation bursts in the outer radiation belt. *Journal of Geophysical Research*, *105*(A7), 15875–15885. https://agupubs.onlinelibrary.wiley.com/doi/abs/10.1029/2000JA900018

Ni, B., Cao, X., Zou, Z., Zhou, C., Gu, X., Bortnik, J., et al. (2015). Resonant scattering of outer zone relativistic electrons by multiband EMIC waves and resultant electron loss time scales. *Journal of Geophysical Research: Space Physics*, *120*(9), 7357–7373. https://doi.org/10.1002/2015JA021466

Pierrard, V., Botek, E., Ripoll, J.-F., & Cunningham, G. (2020). Electron dropout events and flux enhancements associated with geomagnetic storms observed by PROBA-V/energetic particle telescope from 2013 to 2019. *Journal of Geophysical Research: Space Physics*, *125*(12), e2020JA028487. https://doi.org/10.1029/2020JA028487

Reeves, G. D., McAdams, K. L., Friedel, R. H. W., & O'Brien, T. P. (2003). Acceleration and loss of relativistic electrons during geomagnetic storms. *Geophysical Research Letters*, *30*(10), 1529. https://doi.org/10.1029/2002GL016513

Ripoll, J.-F., Claudepierre, S. G., Ukhorskiy, A. Y., Colpitts, C., Li, X., Fennell, J. F., & Crabtree, C. (2020). Particle dynamics in the Earth's radiation belts: Review of current research and open questions. *Journal of Geophysical Research: Space Physics*, *125*(5), e2019JA026735. https://doi.org/10.1029/2019JA026735

Rodriguez, J. V. (2014a). GOES 13-15 MAGE/PD pitch angles algorithm theoretical basis document. Retrieved from https://ngdc.noaa.gov/stp/satellite/goes/documentation.html

Rodriguez, J. V. (2014b). GOES EPEAD science-quality electron fluxes algorithm theoretical basis document. Retrieved from https://ngdc.noaa.gov/stp/satellite/goes/doc/EPEAD_Electron_Science_Reprocessing_ATBD_v1.0.pdf

Scolini, C., Chané, E., Temmer, M., Kilpua, E. K. J., Dissauer, K., Veronig, A. M., et al. (2020). CME–CME interactions as sources of CME geoeffectiveness: The formation of the complex ejecta and intense geomagnetic storm in 2017 early September. *The Astrophysical Journal - Supplement Series*, *247*(1), 21. https://doi.org/10.3847/1538-4365/ab6216

Selesnick, R. S., & Blake, J. B. (2000). On the source location of radiation belt relativistic electrons. *Journal of Geophysical Research*, *105*(A2), 2607–2624. https://agupubs.onlinelibrary.wiley.com/doi/abs/10.1029/1999JA900445

Shen, C., Xu, M., Wang, Y., Chi, Y., & Luo, B. (2018). Why the shock-ICME complex structure is important: Learning from the early 2017 September CMEs. *The Astrophysical Journal*, *861*(1), 28. https://doi.org/10.3847/1538-4357/aac204

Shprits, Y. Y., Horne, R. B., Kellerman, A. C., & Drozdov, A. Y. (2018). The dynamics of Van Allen belts revisited. *Nature Physics*, *14*(2), 102–103. https://doi.org/10.1038/nphys4350

Shprits, Y. Y., Kellerman, A., Aseev, N., Drozdov, A. Y., & Michaelis, I. (2017). Multi-MeV electron loss in the heart of the radiation belts. *Geophysical Research Letters*, *44*(3), 1204–1209. https://doi.org/10.1002/2016GL072258

Shprits, Y. Y., Thorne, R. M., Friedel, R., Reeves, G. D., Fennell, J., Baker, D. N., & Kanekal, S. G. (2006). Outward radial diffusion driven by losses at magnetopause. *Journal of Geophysical Research*, *111*(A11), A11214. https://agupubs.onlinelibrary.wiley.com/doi/abs/10.1029/2006JA011657

Shue, J.-H., Song, P., Russell, C. T., Steinberg, J. T., Chao, J. K., Zastenker, G., et al. (1998). Magnetopause location under extreme solar wind conditions. *Journal of Geophysical Research*, *103*(A8), 17691–17700. https://agupubs.onlinelibrary.wiley.com/doi/abs/10.1029/98JA01103

Sillanpää, I., Ganushkina, N. Y., Dubyagin, S., & Rodriguez, J. V. (2017). Electron fluxes at geostationary orbit from GOES MAGED data. *Space Weather*, *15*(12), 1602–1614. https://doi.org/10.1002/2017SW001698

Staples, F. A., Kellerman, A., Murphy, K. R., Rae, I. J., Sandhu, J. K., & Forsyth, C. (2022). Resolving magnetopause shadowing using multi-mission measurements of phase space density. *Journal of Geophysical Research: Space Physics*, *127*(2), e2021JA029298. https://doi.org/10.1029/2021JA029298

Summers, D., Ni, B., & Meredith, N. P. (2007). Timescales for radiation belt electron acceleration and loss due to resonant wave-particle interactions: 2. Evaluation for VLF chorus, ELF hiss, and electromagnetic ion cyclotron waves. *Journal of Geophysical Research*, *112*(A4), A04207. https://agupubs.onlinelibrary.wiley.com/doi/abs/10.1029/2006JA011993

Thébault, E., Finlay, C. C., Beggan, C. D., Alken, P., Aubert, J., Barrois, O., et al. (2015). International geomagnetic reference field: The 12th generation. *Earth Planets and Space*, *67*(1), 79. https://doi.org/10.1186/s40623-015-0228-9

Thorne, R. M., & Kennel, C. F. (1971). Relativistic electron precipitation during magnetic storm main phase. *Journal of Geophysical Research*, *76*(19), 4446–4453. https://agupubs.onlinelibrary.wiley.com/doi/abs/10.1029/JA076i019p04446

Tsyganenko, N. A. (1989). A magnetospheric magnetic field model with a warped tail current sheet. *Planetary and Space Science*, *37*(1), 5–20. https://doi.org/10.1016/0032-0633(89)90066-4

Turner, D. L., Angelopoulos, V., Morley, S. K., Henderson, M. G., Reeves, G. D., Li, W., et al. (2014). On the cause and extent of outer radiation belt losses during the 30 September 2012 dropout event. *Journal of Geophysical Research: Space Physics*, *119*(3), 1530–1540. https://doi.org/10.1002/2013JA019446

Turner, D. L., Morley, S. K., Miyoshi, Y., Ni, B., & Huang, C.-L. (2012). Outer radiation belt flux dropouts: Current understanding and unresolved questions. In *Dynamics of the Earth's radiation belts and inner magnetosphere* (pp. 195–212).

Turner, D. L., Shprits, Y. Y., Hartinger, M. D., & Angelopoulos, V. (2012). Explaining sudden losses of outer radiation belt electrons during geomagnetic storms. *Nature Physics*, *8*(3), 208–212. https://doi.org/10.1038/nphys2185

Turner, D. L., & Ukhorskiy, A. Y. (2020). Chapter 1 - Outer radiation belt losses by magnetopause incursions and outward radial transport: New insight and outstanding questions from the Van Allen Probes era. In A. N. Jaynes & M. E. Usanova (Eds.), *The dynamic loss of Earth's radiation belts* (pp. 1–28). Elsevier.

Tuszewski, M., Cayton, T. E., Ingraham, J. C., & Kippen, R. M. (2004). Bremsstrahlung effects in energetic particle detectors. *Space Weather*, *2*(10), S10S01. https://doi.org/10.1029/2003SW000057

Usanova, M. E., Drozdov, A., Orlova, K., Mann, I. R., Shprits, Y., Robertson, M. T., et al. (2014). Effect of EMIC waves on relativistic and ultra-relativistic electron populations: Ground-based and Van Allen Probes observations. *Geophysical Research Letters*, *41*(5), 1375–1381. https://doi.org/10.1002/2013GL059024

Usanova, M. E., Mann, I. R., Rae, I. J., Kale, Z. C., Angelopoulos, V., Bonnell, J. W., et al. (2008). Multipoint observations of magnetospheric compression-related EMIC Pc1 waves by THEMIS and CARISMA. *Geophysical Research Letters*, *35*(17), L17S25. https://doi.org/10.1029/2008GL034458

Werner, A. L. E., Yordanova, E., Dimmock, A. P., & Temmer, M. (2019). Modeling the multiple CME interaction event on 6–9 September 2017 with WSA-ENLIL+Cone. *Space Weather*, *17*(2), 357–369. https://doi.org/10.1029/2018SW001993

Xiang, Z., Tu, W., Li, X., Ni, B., Morley, S. K., & Baker, D. N. (2017). Understanding the mechanisms of radiation belt dropouts observed by Van Allen Probes. *Journal of Geophysical Research: Space Physics*, *122*(10), 9858–9879. https://doi.org/10.1002/2017JA024487

Xiang, Z., Tu, W., Ni, B., Henderson, M. G., & Cao, X. (2018). A statistical survey of radiation belt dropouts observed by Van Allen Probes. *Geophysical Research Letters*, *45*(16), 8035–8043. https://doi.org/10.1029/2018GL078907

Xue, Z., Yuan, Z., & Yu, X. (2021). Prompt emergence and disappearance of EMIC waves driven by the sequentially enhanced solar wind dynamic pressure. *Geophysical Research Letters*, *48*(2), e2020GL091479. https://doi.org/10.1029/2020GL091479

Zhang, X.-J., Li, W., Ma, Q., Thorne, R. M., Angelopoulos, V., Bortnik, J., et al. (2016). Direct evidence for EMIC wave scattering of relativistic electrons in space. *Journal of Geophysical Research: Space Physics*, *121*(7), 6620–6631. https://doi.org/10.1002/2016JA022521

Zhao, H., Friedel, R. H. W., Chen, Y., Reeves, G. D., Baker, D. N., Li, X., et al. (2018). An empirical model of radiation belt electron pitch angle distributions based on Van Allen Probes measurements. *Journal of Geophysical Research: Space Physics*, *123*(5), 3493–3511. https://doi.org/10.1029/2018ja025277

References From the Supporting Information

Claudepierre, S. G., Ma, Q., & Bortnik, J. (2022). Quantifying radiation belt electron loss processes at $L < 4$. *Journal of Geophysical Research: Space Physics*, *127*(10), e2022JA030756. https://doi.org/10.1029/2022JA030756